Received: 10 September 2025 | Revised: 28 October 2025 | Accepted: 2 November 2025

DOI: 10.1002/inf2.70104

RESEARCH ARTICLE

WILEY

Perovskite-based time-domain signal-balancing LiDAR sensor with centimeter depth resolution

Gebhard J. Matt[1,2] | **Vitalii Bartosh**[1,2] | **Joshua R. S. Lilly**[3] | **Vincent J.-Y. Lim**[3] | **Lorenzo J. A. Ferraresi**[1,2] | **Daria Proniakova**[1] | **Yuliia Kominko**[1,2] | **Gytis Juška**[4] | **Laura M. Herz**[3] | **Sergii Yakunin**[1,2] | **Maksym V. Kovalenko**[1,2]

[1]Institute of Inorganic Chemistry, Department of Chemistry and Applied Biosciences, ETH Zürich, Zurich, Switzerland

[2]Laboratory for Thin Films and Photovoltaics, Empa – Swiss Federal Laboratories for Materials Science and Technology, Dubendorf, Switzerland

[3]Department of Physics, Clarendon Laboratory, University of Oxford, Oxford, UK

[4]Department of Solid State Electronics, Vilnius University, Vilnius, Lithuania

Correspondence
Sergii Yakunin and Maksym V. Kovalenko, Institute of Inorganic Chemistry, Department of Chemistry and Applied Biosciences, ETH Zürich, Vladimir Prelog Weg 1, CH-8093 Zurich, Switzerland.
Email: yakunins@ethz.ch and mvkovalenko@ethz.ch

Funding information
Innosuisse - Schweizerische Agentur für Innovationsförderung, Grant/Award Number: 46894.1 IP-ENG; Eidgenössische Technische Hochschule Zürich; Engineering and Physical Sciences Research Council

Abstract

A novel class of semiconducting compounds, metal-halide perovskites (MHPs), has emerged as a versatile platform for advanced optoelectronic device architectures, offering a unique combination of exceptional physical properties and facile processing. In this study, we present a monolithic high-speed photodetector capable of directly sensing the time delay between two light pulses with a temporal resolution of at least 170 ps, corresponding to a light propagation distance of ∼5 cm—making it well suited for Light Detection and Ranging (LiDAR) applications. This outstanding time resolution is achieved through a signal-balancing detection scheme that effectively overcomes the limitations of conventional photodetectors, whose response speed is inherently limited by charge-carrier lifetime and transit time. The device exhibits an exceptionally low noise spectral density, comparable to that of state-of-the-art silicon photodiodes. The fully symmetric device stack comprises a crystalline $CsPbBr_3$ absorber layer tens of microns thick, fabricated via a confined melt process. Comprehensive electro-optical characterization reveals charge-carrier lifetimes and mobilities on both microscopic and macroscopic length scales, using transient photoluminescence, time-resolved photocurrent, time of flight, and terahertz pump–probe spectroscopy. The $CsPbBr_3$ layer exhibits charge-carrier lifetimes exceeding 100 ns, a microscopic electron–hole mobility of 15 ± 1 $cm^2\ V^{-1}\ s^{-1}$, and a macroscopic non-dispersive hole mobility of 8.5 $cm^2\ V^{-1}\ s^{-1}$.

KEYWORDS

balanced photodetectors, LIDARS, metal halide perovskites, photodetectors, time of flight

1 | INTRODUCTION

Fast optical sensing is crucial across a wide range of technologies, with Time-of-Flight (ToF) rangefinders—commonly known as Light Detection and Ranging (LiDAR)—representing one of the most prominent and rapidly advancing examples.[1] In LiDAR systems, distance is determined from the time delay between emitted and detected light pulses. However, environmental factors can distort the temporal profile of the returning signal, necessitating high-speed sampling and extensive post-processing to recover accurate distance information from complex photon-count distributions.[2]

In this work, we introduce an alternative two-beam detection scheme employing a monolithic photodetector architecture that directly measures the *relative time delay* between two light pulses (Figure 1A). As a differential detection method, this approach efficiently suppresses common-mode disturbances affecting both beams. The concept is realized in a fully symmetric photodetector with transparent electrodes on both sides, allowing simultaneous optical excitation from opposite directions (Figure 1D). In this "*balanced operational mode*," the external photocurrent varies in polarity and magnitude with the relative time delay between the two optical pulses (Figure 1A,E–G), enabling LiDAR-like operation with a demonstrated temporal resolution of 170 ps, corresponding to a light-propagation distance of ~5 cm. Importantly, in this mode the photocurrent response is no longer limited by the charge-carrier transit time or lifetime within the absorber.

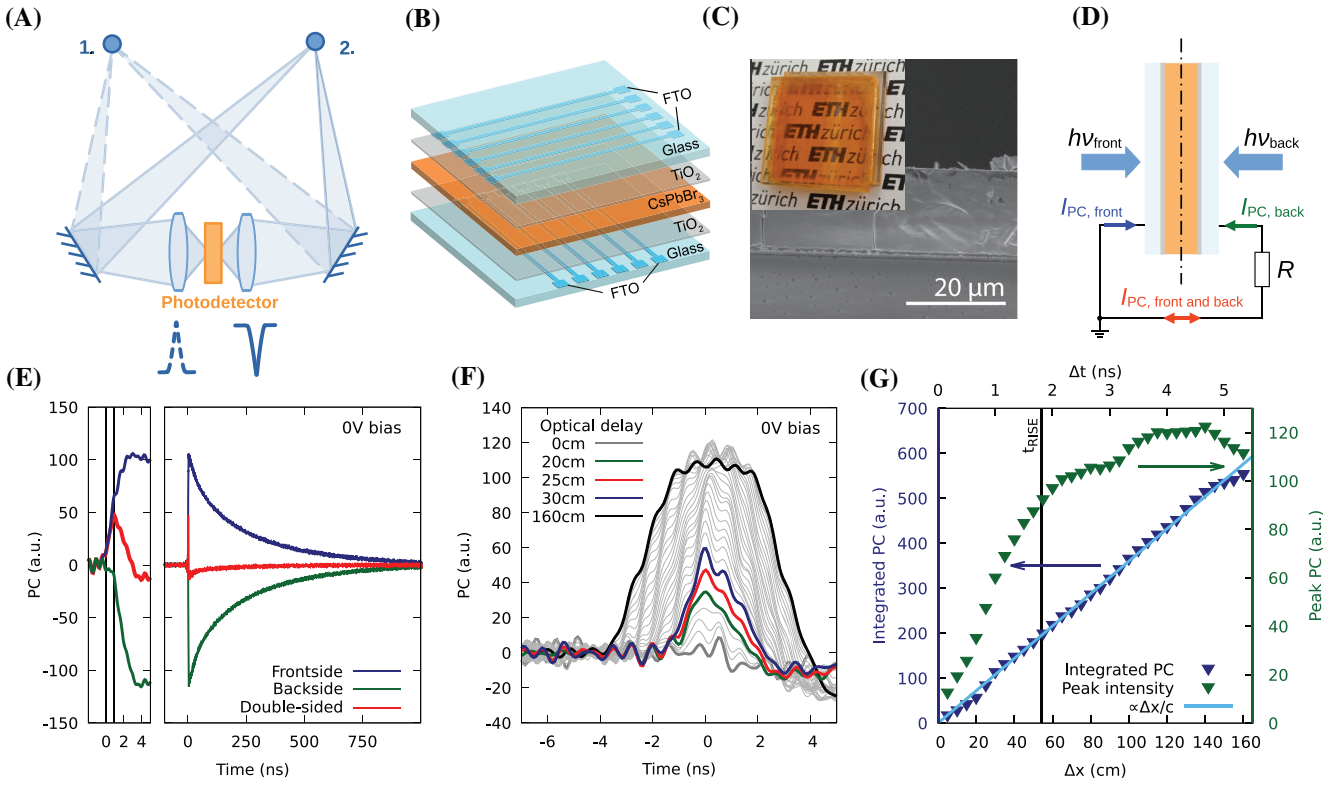

FIGURE 1 Device stack and the "balanced operational mode". (A) The photodetector, represented as a brown bar, receives light collected from opposite sides. The resulting photocurrent varies in both polarity and intensity, depending on the difference in the lengths of the individual optical paths—indicated by the dashed and solid lines originating from positions 1 and 2, respectively. (B) The device stack consists of two identical top and bottom glass substrates, each coated with fluorine-doped tin oxide (FTO, ~100 nm) and titanium dioxide (TiO_2, ~70 nm) and a crystalline metal-halide perovskite middle layer of $CsPbBr_3$ (17 µm). The FTO is electrochemical etched to 0.5 mm wide stripes. The top and bottom substrates are rotated by 90° to define a crossbar configuration. (C) Scanning electron microscopy showing the cross-section of the crystalline $CsPbBr_3$ layer. The inset is a photograph of the semi-transparent photodetector. (D) Schematics of the photodetector with pulsed optical excitation on both sides. The transient photocurrents (tr-PC) are indicated as blue, green and red arrows. (E) tr-PCs after optical excitation with a ps-laser (488 nm, 6.5 pJ, 1.5 kHz repetition rate) measured at 0 V bias in the photovoltaic mode. The frontside and backside are shown in blue and green, respectively. The relative time difference of the individual excitations is $\Delta t = 0.83$ ns. "balanced operational mode"—The red trace shows the tr-PC after frontside and backside excitation with the same relative time delay Δt. The left panel in (E) magnifies the tr-PCs and Δt is marked as vertical dotted lines. (F) tr-PCs with different time delays of the frontside and backside excitations. (G) Integrated tr-PCs and the peak tr-PCs amplitudes versus $\Delta x = c\Delta t(x)$ is shown as blue and green triangles respectively. The light blue line indicates the proportionality of the integrated tr-PC versus optical delay Δx.

Instead, a single residual transient photocurrent directly measures the optical time delay (Figure 1F,G). As a result, the external readout circuitry can operate without high-speed sampling (i.e., simple charge-integrating amplifier)—yielding a compact, monolithic, and inherently robust detection concept.

The operating principle of this photodetector differs fundamentally from classical *p-i-n*-photodiodes. Rather than relying on charge extraction, it is governed by the rapid spreading of spatially narrow non-equilibrium space-charge distributions within the photoactive layer. As the absorber, a tens-of-microns-thick $CsPbBr_3$ metal-halide perovskite (MHP) layer is employed, fabricated via a custom-designed confined melt process between two conductive, optically transparent substrates. MHPs are ideally suited for this architecture owing to their combination of key optoelectronic properties—high absorption coefficient, tuneable bandgap, and excellent charge-transport characteristics.[3–5] In addition, they exhibit exceptional defect tolerance[6] and compatibility with scalable, low-cost processing techniques,[7] establishing them as a versatile materials platform for advanced optoelectronic devices, including solar cells,[8] hard-radiation detectors,[9–13] color-sensitive sensors,[14] and fast photodetectors.[15,16] It is emphasized, that the specific combination of material properties enabling this photodetector concept is difficult to achieve with conventional semiconductors. The indirect bandgap of silicon prevents the formation of sharp space-charge gradients, while the extremely high carrier mobility in direct-bandgap III–V semiconductors shifts the response into the terahertz regime, beyond the reach of conventional electronic detection.[17,18]

We also complement this work with a comprehensive optoelectronic characterization of the melt-processed $CsPbBr_3$ layers, assessing charge-carrier lifetimes and mobilities across microscopic and macroscopic scales using transient photoluminescence, time-resolved photocurrent, time-of-flight, and optical-pump microwave/terahertz probe spectroscopies. The results reveal non-dispersive hole transport, with a total microscopic electron–hole mobility ($\mu_{\text{total}} = 15 \pm 1\ \text{cm}^2\ \text{V}^{-1}\ \text{s}^{-1}$) only twice the macroscopic hole mobility, while the hole lifetimes are found to be consistent across all techniques ($\tau > 100$ ns). Furthermore, the photodetector exhibits an exceptionally low noise spectral density, comparable to that of modern silicon photodiodes.

2 | RESULTS AND DISCUSSION

The fast photodetector features a fully symmetric device stack (Figure 1B), comprising a tens-of-microns thick inorganic metal-halide perovskite $CsPbBr_3$ layer sandwiched between two identical transparent electrodes. $CsPbBr_3$ was chosen for its chemical and structural stability, as well as its ability to form a thermodynamically stable liquid phase near 570°C, enabling single-crystal growth via the Bridgman–Stockbarger[19,20] method and even direct melt deposition onto substrates.[12] Owing to its excellent charge-transport properties and strong stopping power for high-energy radiation, $CsPbBr_3$ has been widely employed in x-ray and γ-ray detectors. However, due to its wide bandgap (2.36 eV), $CsPbBr_3$ is less suitable for photovoltaic applications but remains attractive for photodetector applications, as it combines a low intrinsic free carrier concentration with a high optical absorption coefficient. Figure 2A shows the absorption spectrum and the corresponding Tauc plot after Zanatta et al.,[21] confirming an absorption coefficient of $\sim 2 \times 10^4\ \text{cm}^{-1}$ at the band edge.

A key feature of this fully symmetric photodetector architecture, with transparent electrodes on both sides, is its ability to be optically excited from either one or both sides. The general behavior under single- and double-sided excitation is discussed first, followed by the device fabrication process. Particular emphasis is placed on the double-sided, or "*balanced operational mode*," which is especially relevant for LiDAR applications. The *Results* section concludes with a comprehensive electro-optical characterization, detailing the charge-carrier dynamics and overall device performance.

A *single*-sided optical excitation leads to a transient photocurrent (tr-PC) characterized by a fast rise, that is, $\tau_{rise} = 1.7$ ns, followed by an exponential decay with a time constant $\tau > 100$ ns (Figure 1E). As detailed in Supporting Information Note 1, the tr-PC can be described as the sum of two exponentials of opposite polarity:

$$I_{\text{tr-PC}}(t) = \frac{I_0}{1 - \tau_{rise}/\tau}\left[\exp\left(-\frac{t}{\tau}\right) - \exp\left(-\frac{t}{\tau_{rise}}\right)\right]; \quad (1)$$

where τ is the hole lifetime and τ_{rise} is a rise time constant. Figure S5A shows an experimental confirmation that $\tau_{rise} = RC$ where C is the device capacitance and R is the resistive load. Therefore, minimizing C is essential for achieving a fast photoresponse. This can be achieved either by increasing the photoactive layer thickness or by reducing the contact area. However, while smaller contacts effectively lower C, they also lead to proportionally smaller photocurrents.[16] In this work, we employed the strategy of a thick photoactive layer by introducing a custom developed confined melt-processing of the metal-halide $CsPbBr_3$, yielding crystalline layers with thicknesses in the order of tens-of-microns.

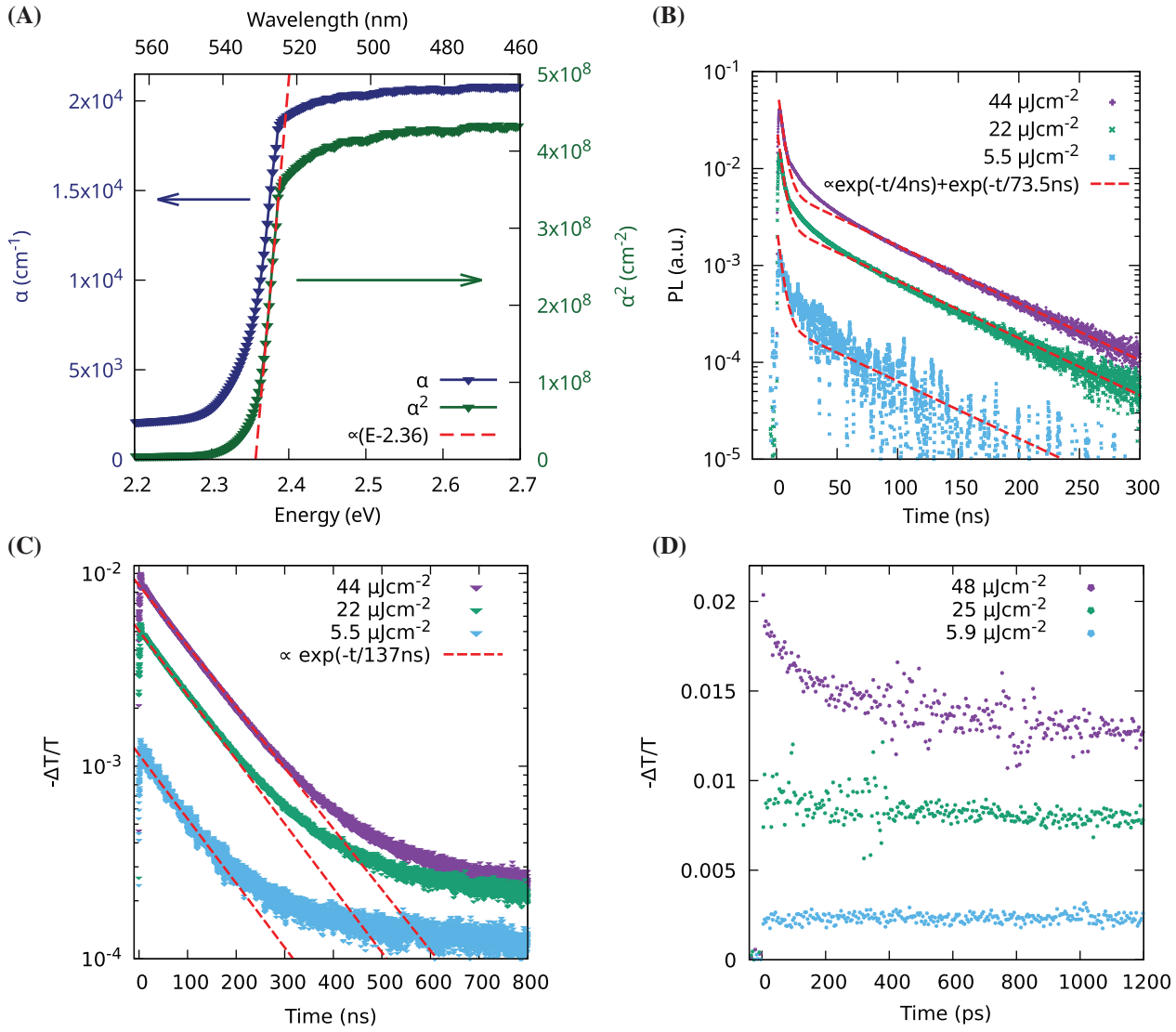

FIGURE 2 Absorption, transient photoluminescence and optical-pump and microwave/THz probe spectroscopy. (A) Absorption spectrum in blue and a "Tauc" plot after Zanatta et al. in green.[21] (B) Transient photoluminescence at three different fluences. The dashed red lines are bi-exponential fits with the fluence-independent time constants of 4s and 73.5 ns, respectively. (C, D) Optical-pump and microwave/THz probe spectroscopy. The probe is microwave radiation (102 GHz) in (C) and THz radiation in (D). The solid lines in (C) are an exponential fit with a fluence-independent time constant of 137 ns. The sum of the microscopic electron and hole mobilities can be ascertained in (D) from the onset at $t = 0$. Optical excitation in (B, C, D) with an fs laser (35 fs, 400 nm, 5.5–44 μJ cm^{-2}, 5 kHz repetition rate).

A *double*-sided excitation generates two independent transient photocurrents (tr-PCs) of opposite polarity. The opposite polarity arises directly from the full device symmetry and the shared connection through a single load resistor (R). The two external tr-PCs partially cancel each other, described by: $I_{\text{residual}} = I_{\text{PC-frontside}} - I_{\text{PC-backside}}$ (red arrow in Figure 1D), with the residual tr-PC measured as a voltage drop across the common load resistor R (red trace). Such double-sided excitation scheme, hereafter referred to as the "balanced operational mode" is a differential measurement that is highly sensitive to the time correlation (i.e., time delay) between the two optical excitations. In the context of LiDAR applications, this enables highly precise optical distance measurements.

The "balanced operational mode" critically depends on identical temporal responses from both optical excitations. This is achieved by a strictly symmetric device architecture, realized by embedding the photoactive layer between two identical, transparent, electrode-coated substrates. It is emphasized that the tr-PCs are sensitive to an external electric field and consequently, the "balanced operational mode" is achieved only in a symmetric device stack operating under short-circuit in the photovoltaic mode.

2.1 | Fabrication of the LiDAR device by confined melt processing of $CsPbBr_3$

Following the stringent requirement of a fully symmetric device architecture, the $CsPbBr_3$ layer is fabricated in a single processing step via a confined melting of $CsPbBr_3$ between two identical substrates. The detailed fabrication sequence is provided in the Experimental Section and summarized in the flowchart shown in Figure S2. In brief, microcrystalline $CsPbBr_3$ powder was placed between two substrates and heated in an oven to its melting point (~570°C). The substrates are fluorine-doped tin oxide (FTO, ~100 nm) coated glass slides (1 inch × 1 inch) with an additional TiO_2 layer (~70 nm). The FTO electrodes were electrochemically etched[22] into 0.5 mm-wide stripes, and the substrates were rotated by 90° to form a crossbar configuration, defining an active device area of 0.5 × 0.5 mm^2. Video S1 demonstrates the homogeneous melt distribution and the remarkably rapid crystallization within ~3 s, due to a strongly undercooled melt.[23] The resulting $CsPbBr_3$ layer is 17 μm thick, laterally polycrystalline, and single-crystalline across the film (Figure 1C). Detailed crystallographic investigations have been reported previously,[12] confirming large phase pure orthorhombic crystalline domains with the *c*-axis of the unit cell close to the surface normal. It is noted that the photodetector exhibited excellent environmental stability, as the $CsPbBr_3$ layer is embedded between two glass substrates, providing highly effective encapsulation from ambient conditions. All experimental work was performed under ambient atmosphere, without the use of an additional sample chamber, over a period of several months.

2.2 | LiDAR operation under "*balanced operational mode*"

In the "*balanced operational mode*," the tr-PC exhibits a fast rise and decay in the nanosecond regime, effectively suppressing the slow decay observed in individual tr-PCs. Figure 1E shows a representative tr-PC trace (red) recorded with a relative time delay of $\Delta t = 0.83$ ns (equivalent to 25 cm of light propagation) between the two optical excitations. The tr-PC rise is following the initial excitation (blue trace) and the decay is following the delayed excitation (green trace). Figure 1F presents a series of tr-PC traces obtained as the optical delay (Δx) was varied in 5 cm increments ($\Delta t = 167$ ps). A schematic of the experimental setup is provided in Figure S6. An analysis of the peak amplitudes (green triangles) and numerically integrated tr-PC signals (blue triangles) is summarized in Figure 1G. With increasing optical delay, the peak amplitudes increase rapidly until the optical delay approaches the rise time of the individual tr-PCs. The numerically integrated tr-PC vs. optical delay shows a strict linear dependency (see Figure S7 for a mathematical proof). This linearity represents a *key result* with direct relevance for LiDAR applications, as the charge-integration of the tr-PC signal can be readily implemented using a charge-integrating amplifier. This behavior is also considered the main distinction from recent work on fast perovskite photodetectors[15,16] relying on thin-film low-area devices,[15,16] although those studies report higher temporal resolutions. For our devices, higher temporal resolutions are achievable, but currently experimentally limited by the oscilloscope's sampling rate (12.5 GSs^{-1}, corresponding to 80 ps between samples).

2.3 | Electro-optical characterization

In the following two sections, optical pump microwave/THz-probe spectroscopy, time-of-flight charge transport measurements and noise measurements are presented, aimed at elucidating the photocurrent generation and the dynamics of photoexcited charge carriers.

2.3.1 | Transient photoluminescence and optical-pump and THz-probe (OPTP) and time-resolved microwave conductivity (TRMC)

Experimental details of the OPTP and TRMC measurements been described in previous publications.[24–27] In brief, the samples were optically pumped using a femtosecond Ti:Sapphire laser system and probed either with microwave radiation (102 GHz, time-resolved microwave conductivity, TRMC) or with terahertz radiation (optical-pump terahertz-probe, OPTP) generated by a tri-layer spintronic emitter.[28] The pump operated at a repetition rate of 5 kHz. Transient photoluminescence was measured in situ alongside the pump-probe experiments, enabling an accurate comparison of their respective temporal responses. For a precise comparison with the transient photocurrent measurements, the samples used for the pump-probe experiments were prepared identically, except that *z*-cut quartz plates were employed instead of TiO_2/FTO-coated glass substrates. Figure 2C,D show the normalized change in transmission $-\Delta T/T$ probed by microwave radiation in Figure 2C and probed by THz radiation in Figure 2D. In both experiments, $-\Delta T/T$ is proportional to the photoconductivity $eN(t)\mu_{total}$, where N is the number of photoexcited charge-carriers and e is the elementary charge, while $\mu_{total} = \mu_e + \mu_h$ is the sum of the microscopic electron and hole mobilities. The Time-

Resolved Microwave Conductivity (TRMC) traces shown in Figure 2C feature a predominantly fluence independent single-exponential decay with a time constant of 137 ns. Sub-ns charge-carrier dynamics is investigated by Optical-Pump and THz-Probe (OPTP). The sub-ns time resolution allows an accurate determination of μ_{total} before significant recombination occurs and it has been shown that μ_{total} is related to $-\Delta T/T$ (when the probe wavelength is much larger than the film thickness) by[24,29]:

$$\mu_{total} = -\frac{\epsilon_0 c(n_A + n_B)A_{eff}}{eN}\frac{\Delta T}{T}; \quad (2)$$

where ϵ_0 is the vacuum permittivity, c is the speed of light, $n_{A,B}$ are the refractive indices in the THz regime for the media at either side of the $CsPbBr_3$ film (z-cut quartz for the present sample) and A_{eff} is the effective area of the overlap between the THz probe and the optical-pump. Using Equation (2), a total microscopic mobility $\mu_{total} = 15 \pm 1\ cm^2 V^{-1} s^{-1}$ is ascertained from the onset in Figure 2D at $t = 0$.

2.3.2 | Free charge-carrier lifetime, time-of-flight, and noise spectroscopy

Figure 3A shows the tr-PC measured under the same experimental conditions as in Figure 1E, but with a variation of the laser excitation repetition rate f from 500 Hz to 10 kHz. The change in repetition rate predominantly changes the decay dynamics. For $f < 2$ kHz the decay features two exponential time constant τ_0 and τ_1, whereas for $f > 2$ kHz, the decay is single exponential with a 6-fold smaller τ_1 and a 2.2-fold increase in peak amplitude at $f = 10$ kHz. Figure 3B summarizes τ_0 and τ_1 as a function of the repetition rate.

Another property of this photodetector is its exceptionally low noise spectral density. The noise spectral density is $N_S = 9$ to $6.5 \times 10^{-16}\ Hz^{-0.5}$ between 100 Hz and 1 kHz at 0 V bias (Figure 3D). See Experimental Section in the Supporting Information for the details.[30] A discussion of the figure-of-merit—the specific detectivity D^*—is presented in Supporting Information Note 2, where the estimated value is found to be competitive. The noise level is that low, as it is dominated by the Johnson–Nyquist noise, which is limited by the extremely low thermally excited free charge-carrier concentration in $CsPbBr_3$. However, with applied bias, the noise increases significantly due to the charge injection. An asymmetric device stack would suppress charge injection (e.g., n-p selective electrodes) but this would prevent the "balanced operational mode"—which requires a fully symmetric device stack and as such, it must operate in the photovoltaic mode at a 0 V bias.

To further investigate the charge transport, a bias is applied. Upon sufficient high bias, the free charge-carrier drift distance is approaching the sample thickness, thereby enabling the conditions of the Time-of-Flight (ToF) method. ToF is the most direct method of measuring the drift-mobility μ, as it directly measures the drift-velocity $v = \mu \cdot E$ of the charge-carriers after an optical excitation, where E is the electric field. Although it is a classic and well-established method, ToF on MHPs requires several precautions. The electric field is alternating to prevent field screening due to ion migration[3] and the excitation intensity must be reduced to a value such that the total photoexcited charge is $Q < CV$[31]; where C is the sample capacitance and V is the bias voltage applied at the time of the optical excitation. A well-resolved ToF transient requires (and points to) a non-dispersive charge transport, charge-carrier lifetime longer than transit-time τ_{tr}, and high electronic resistivity. The latter is a necessary condition for ToF applicability, since the transit-time τ_{tr} of the charge-carriers must be shorter than dielectric relaxation time $\tau_d = \kappa r$; where κ is the dielectric constant and r is the resistivity.[32] Figure 4A,B show the transient photocurrent traces at different bias voltages. In Figure 4A, the bias voltage V is varied between -1 and $+1.5$ V and in Figure 4B,V is varied between 0 and -10 V. The tr-PC signal is enhanced under negative bias and suppressed under positive bias at the non-illuminated electrode, indicating that the tr-PC under bias is a bulk hole drift current. In general, the photocurrent j is described by the Ramo theorem, which states that an external current is induced by the motion of charge-carriers in an electric field E. Specifically, $j = envd$; where n is the sheet density of charge-carriers, v is their drift velocity, and d is the distance between the electrodes. The sharp drop of j in Figure 4B is at the time $\tau_{tr} = d/v$, when the charge-carriers reach the collecting electrode and provide a direct measure of the drift mobility by $\mu = d/(\tau_{tr}E)$. An ideal time-of-flight (ToF) transient exhibits characteristic scaling behavior versus applied bias: the tr-PC amplitude at the transit-time (j_{tr}) increases proportionally with bias, while the transit-time τ_{tr} decreases inversely with it. Hence, the product of these two parameters is a constant, and this scaling: $j_{tr} \propto 1/\tau_{tr}$ is indicated as red dashed line in Figure 4B. In this bias regime ($V > \sim 4.5$ V), the hole mobility can be precisely measured and reads as $\mu_h = 8.5\ cm^2 V^{-1} s^{-1}$ (Figure 4C, non-valid mobility values are marked in gray). This mobility value is in the same order as reported values in Bridgman grown $CsPbBr_3$ single crystals[33–35] and a Table S1 for a comparison. Figure 4D shows the numerically time-integrated tr-PC traces Q versus V. Beyond

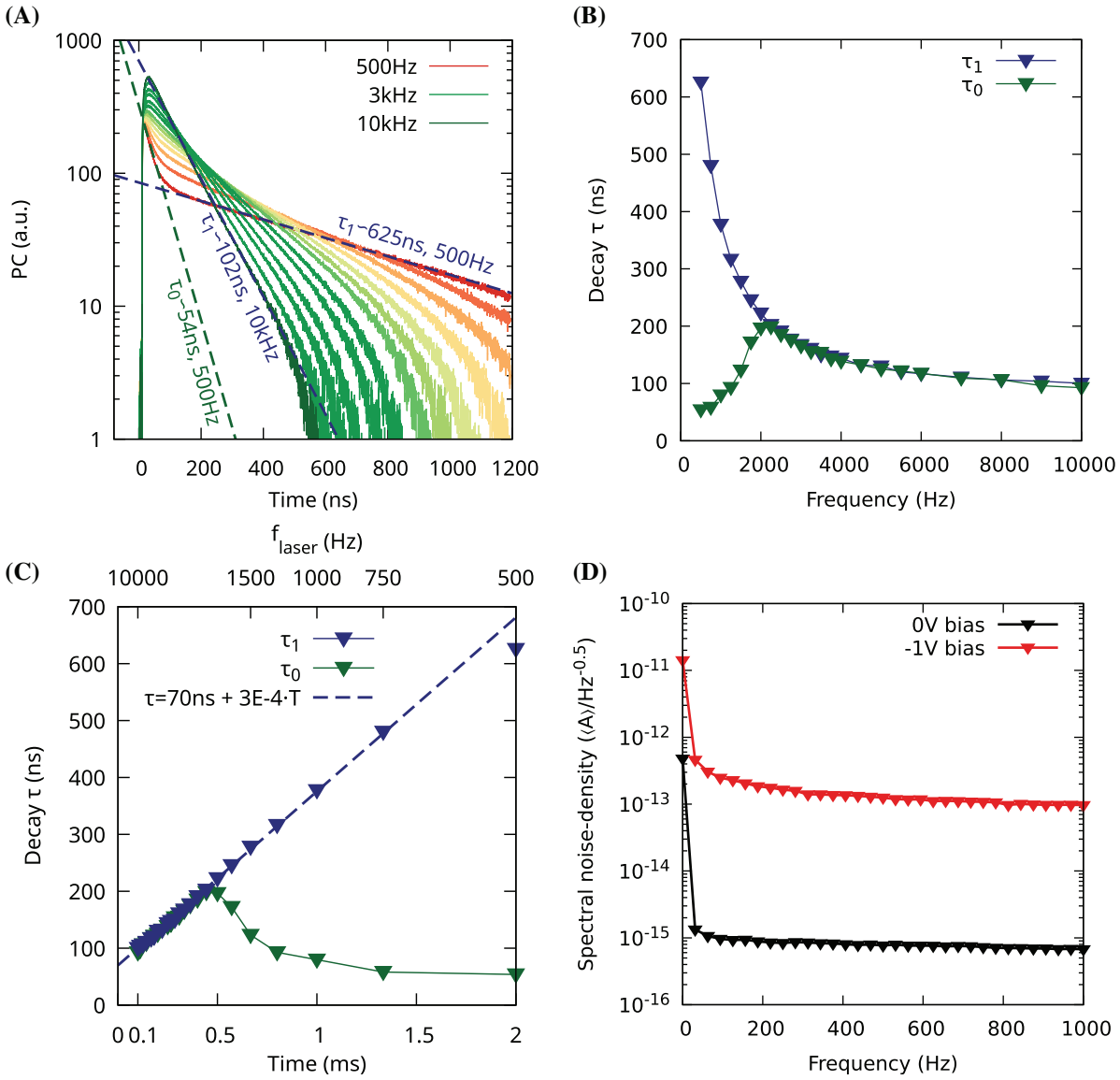

FIGURE 3 Transient photocurrents at 0 V bias and noise spectral density. (A) Transient photocurrent at different repetition rates of excitation f varied from 500 Hz to 10 kHz. τ_0 and τ_1 are exponential fits after excitation and at short and longer timescales, respectively. (B) Exponential decay time constant τ_0 and τ_1 versus f obtained from (A). For $f > 2$ kHz, τ_0 equals τ_1. (C) Replot of (B) showing τ_0, τ_1 versus the time $T = 1/f$ between the optical excitations. (D) Noise spectral density at 0 V and −1 V bias, respectively.

−3.5 V bias, the collected charge Q saturates, indicating that the charge-carrier extraction efficiency approaches unity. The saturation of Q versus V enables the calculation of a $\mu\tau$ product. The $\mu\tau$ product is the figure-of-merit of a photoconductor, as it defines the carrier Schubweg $S = \mu\tau E$, the mean carrier drift distance before a charge is trapped or recombined. Following Kočka et al.[36] a $\mu\tau$ product is determined from a double logarithmic graph of Q versus V through the crossing point of two tangents drawn to its rising and saturating parts. This crossing point defines a specific bias voltage V_h for which S equals d, and the $\mu\tau$ product is given by $\mu\tau = d^2/V_h$. The inset in Figure 4D shows this approach, and the $\mu\tau$ product for holes reads as $\mu\tau = 2 \times 10^{-6}$ cm^2 V^{-1}; with $d = 17\,\mu$m and $V_h = 1.5$ V. The hole lifetime derived from this $\mu\tau$ product is $\tau = 235$ ns and is in excellent agreement with the $\tau = 280$ ns obtained from the tr-PC transients at the same excitation rate of 1.5 kHz (Figures 3B and S5B). The evaluated $\mu\tau$ product is not among the highest reported number for similar materials, but it confirms excellent overall performance as demonstrated by the non-dispersive ToF transients, a charge extraction efficiency of ∼8% at 0 V bias and a unity charge extraction efficiency at a bias of just a few volts.

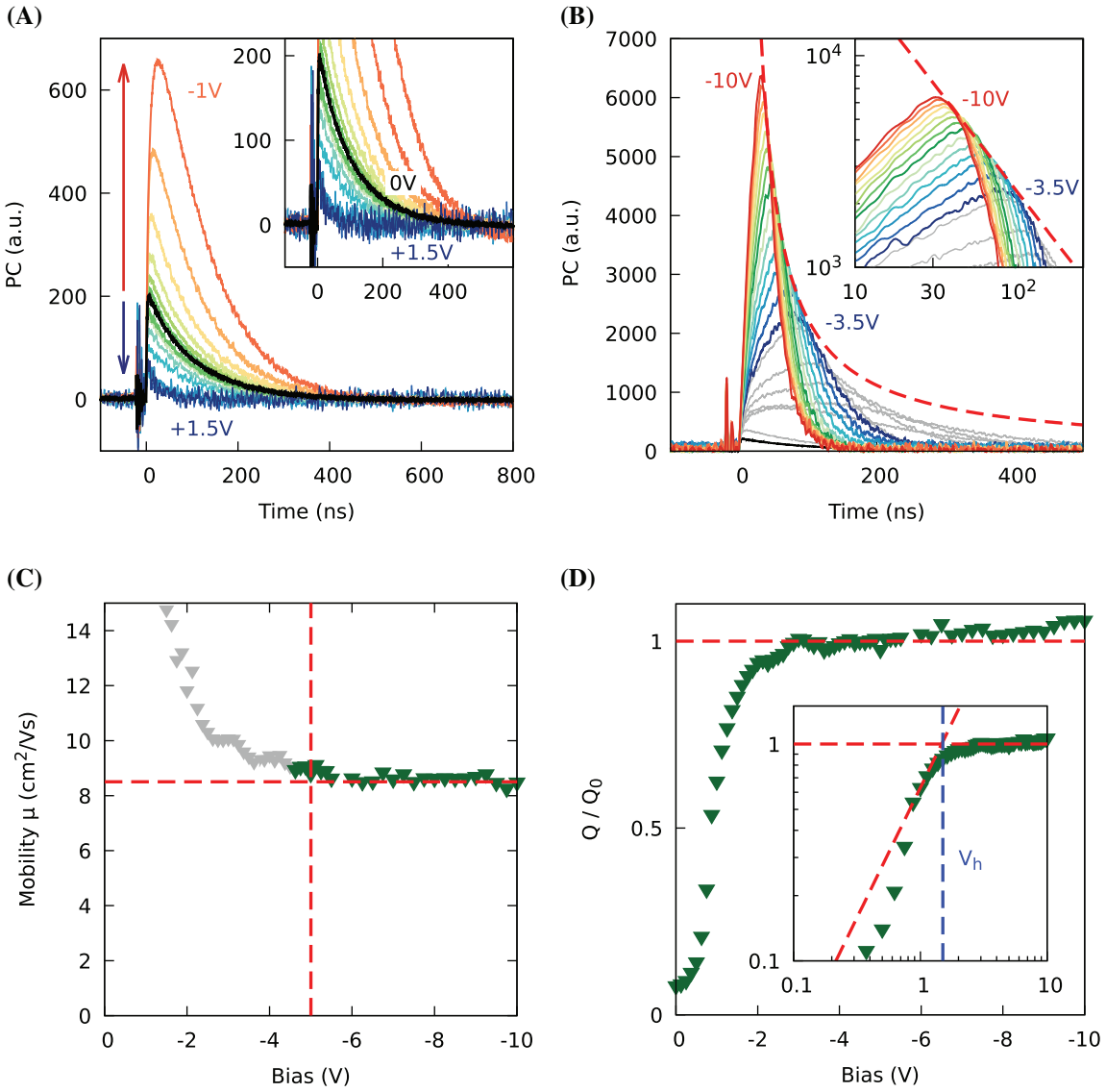

FIGURE 4 Transient photocurrents with applied bias and the Time-of-Flight method. (A) The bias is varied in 125 mV steps from −1 to +1.5 V. The transient photocurrents are enhanced for negative bias potentials (red arrow) and are quenched for positive bias potentials (blue arrow) at the non-illuminated electrode. The 0 V bias is shown in black. *Time-of-Flight method*: (B) the bias is varied in steps of 0.5 V from 0 to −10 V. The dashed red line marks the constant product of the amplitude with the onset of the decay, and the inset replots with double logarithmic axes. (C) Bias dependence of the hole mobility. The green triangles indicate the valid mobility values extracted from transient photocurrents that follow the scaling behavior shown by the dashed red line in (B). (D) Bias dependence of the numerically integrated tr-PC traces from (B). The inset shows the same data on double logarithmic axes, allowing determination of V_h, where the hole drift distance equals the sample thickness.

2.3.3 | Summary of the electro-optical characterization

A particularly notable feature observed across the transient photoluminescence (tr-PL), transient photocurrent (tr-PC), and pump-probe measurements is the consistent appearance of fluence-independent single-exponential decays. Such first-order recombination kinetics are characteristic of semiconductors in which recombination is governed by a single type of charge carrier. This combined with the fact that tr-PC selectively probes macroscopic hole transport, strongly suggests rapid and deep trapping of electrons.[23]

The tr-PC decay time constant (τ_1) depends sensitively on the repetition rate of the optical excitation (Figure 3A,B). As shown in Figure 3C, τ_1 is strictly proportional to the time interval between optical excitation ($T = 1/f$), following a linear relationship: $\tau_1 = \tau_\infty + aT$ where $\tau_\infty = 70\,\text{ns}$ and $a = 3 \times 10^{-4}$. This linear dependency is attributed to a shallow trap filling process.

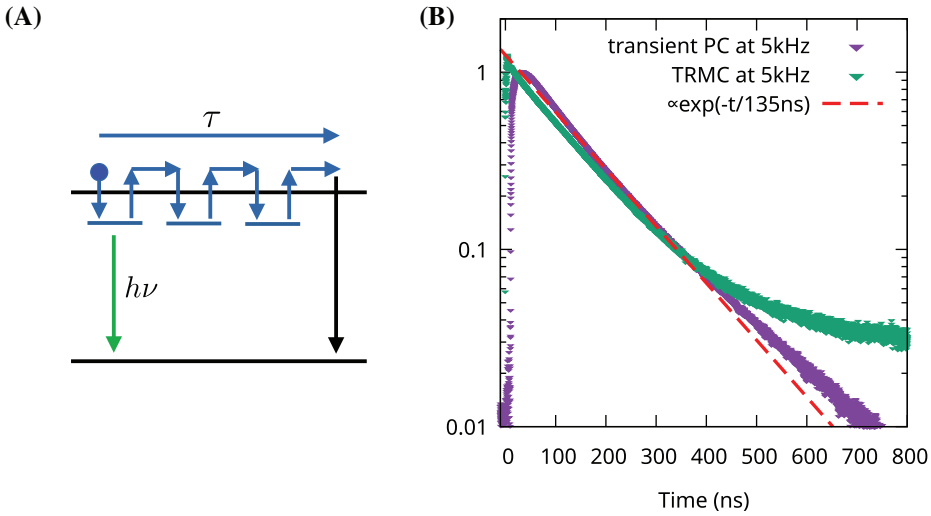

FIGURE 5 (A) Multiple shallow trapping process. Radiative and non-radiative recombination are indicated by green and black arrows, respectively. For the sake of illustration, the trapping process is shown for electrons, while for $CsPbBr_3$ (as a hole conductor) it is only valid for holes. (B) Comparison of the transient photocurrent (tr-PC) with Time-Resolved Microwave Conductivity (TRMC). In both experiments, the repetition rate of the optical excitation was 5 kHz, and identically prepared $CsPbBr_3$ films were used; however, the TRMC measurements were performed on samples without electrodes. Despite the significant difference in excitation intensity (488 nm, 40–90 ps, 6.5 pJ for the tr-PC vs. 400 nm, 35 fs, 44 μJ cm^{-2} for the TRMC), the decay shows an identical time constant of ∼135 ns.

Charge transport under shallow trapping was first introduced by Hornbeck and Haynes[37] who proposed a multiple capture and thermally re-emission from shallow traps. In the limit of long timescales, the free charge-carrier concentration decays single-exponentially, with a time constant linearly dependent on the density of empty traps (N_e):

$$\tau = \tau_f + kN_e; \tag{3}$$

where τ_f is the carrier lifetime in the low-trap-density limit, and k quantifies the repeated capture and thermal release processes from shallow traps (see Supporting Information Note 3 for further discussion). In the limit of full trap filling (i.e., $N_e = 0$), τ approaches τ_f and is determined from the vertical onset in the linear fit in Figure 3C as $\tau = 70$ ns. A remarkably similar time constant is observed as the slow exponential decay component in tr-PL with $\tau_r = 73.5$ ns, Figure 2B. Based on this, the slow tr-PL decay is interpreted as the radiative recombination of holes not involved in the shallow-trapping process (see schematic in Figure 5A). The fast initial tr-PL decay in Figure 2B with a time constant of ∼4 ns is an excitonic emission, commonly observed in $CsPbBr_3$ nanostructures,[38] or with more complex processes such as carrier diffusion and photon reabsorption in optically thick films.[39,40]

It is summary, the carrier dynamics and transport measured electrically by transient photocurrent and Time-of-Flight, optically by transient photoluminescence, and by optical-pump and microwave/THz probe are in excellent agreement. Such consistency is only possible because the $CsPbBr_3$ films studied are crystalline and of excellent quality. The similarity of microscopic and bulk charge transport is best illustrated by the observation, that the sum of the microscopic electron and hole mobility measured by optical-pump and THz probe spectroscopy is only a factor of two higher than the macroscopic hole mobility measured by Time-of-Flight.

2.3.4 | Origin of the photocurrent

The symmetry-breaking $TiO_2/CsPbBr_3$ heterojunction plays a crucial role in photocurrent generation. TiO_2 surfaces are strong electron acceptors, and various TiO_2 phases are widely used in perovskite and dye-sensitized solar cells.[41,42] The importance of TiO_2 is clearly demonstrated in Figure S3, which shows a pronounced increase in short-circuit photocurrent upon introducing a TiO_2 interlayer.

As illustrated schematically in the energy diagram in Figure S9, the lower work function of TiO_2 relative to the conduction band of $CsPbBr_3$ establishes a strong interfacial electric-field gradient directed toward the TiO_2. This field facilitates efficient exciton dissociation, promotes electron injection into TiO_2, and results in an excess hole concentration within the $CsPbBr_3$ layer.

The identical temporal responses observed in transient photocurrent (tr-PC) and time-resolved microwave

conductivity (TRMC) measurements (Figure 5B) indicate that the lifetime of excess free charge-carriers in $CsPbBr_3$ is not affected by the $TiO_2/CsPbBr_3$ heterojunction. This finding suggests that the tr-PC originates solely from electron–hole separation at the heterojunction, without significant contribution from excess charge-carriers within the bulk $CsPbBr_3$ (i.e., within the optical penetration depth). Under short-circuit conditions, owing to the symmetric device architecture, no macroscopic electric field is present across the $CsPbBr_3$ layer. Consequently, the steeply decaying and spatially confined space-charge distribution of the excess carriers, combined with the absence of an external electric field, leads to their redistribution into the bulk predominantly by ambipolar diffusion. When an external bias is applied, however, the additional macroscopic electric field strongly influences the photocurrent (Figure 4A,B) through enhanced hole drift. This is consistent with the observation that a bias of only 1.5 V is sufficient to achieve a hole drift length equal to the sample thickness (Figure 4D). Such extended drift lengths, exceeding typical diffusion lengths even at low bias, are characteristic of highly crystalline semiconductors with excellent charge-transport properties.[43,44]

3 | CONCLUSION

A novel high-speed photodetector based on non-equilibrium, spatially confined space-charge distributions within a metal-halide perovskite ($CsPbBr_3$) absorber is presented. The device features a fully symmetric architecture incorporating a tens-of-microns thick crystalline $CsPbBr_3$ layer, enabling optical excitation from both sides. Under double-sided excitation—referred to as the balanced operational mode—the photocurrent directly and precisely measures the time delay between two optical pulses. This functionality arises from the exceptional material properties of $CsPbBr_3$, including its high absorption coefficient and excellent charge-transport characteristics. The photodetector response is independent of the intrinsic charge-carrier lifetime and transit time, thereby overcoming the extraction-time limitations of conventional photodiodes. The resulting monolithic architecture is inherently simple and achieves sub-nanosecond response times, with a demonstrated temporal resolution of 170 ps, corresponding to a light-propagation distance of ∼5 cm. Beyond its immediate relevance to LiDAR and high-speed optical sensing, this concept establishes a general framework for integrating time-resolved functionality into perovskite-based and other emerging semiconductor technologies.

Comprehensive electro-optical characterization of the $CsPbBr_3$ layers further supports these findings. Charge-carrier dynamics were investigated using transient photoluminescence, time-resolved photocurrent, time-of-flight, and optical-pump microwave/terahertz probe spectroscopies. The material exhibits non-dispersive hole transport with a macroscopic mobility of 8.5 $cm^2\ V^{-1}\ s^{-1}$, while the total microscopic electron–hole mobility ($\mu_{total} = 15 \pm 1\ cm^2\ V^{-1}\ s^{-1}$) differs by only a factor of two from the macroscopic value. The hole lifetime was found to be consistent across all techniques ($\tau > 100$ ns). A shallow-trapping model is introduced, providing a unified framework that links radiative and non-radiative recombination dynamics.

4 | EXPERIMENTAL

4.1 | Sample preparation

Includes (1) $CsPbBr_3$ synthesis, (2) substrate preparation, (3) the confined melting of $CsPbBr_3$. A flowchart illustrating the preparation steps of the LiDAR photodetector is provided in Figure S2.

1. *$CsPbBr_3$ synthesis*: Cesium bromide CsBr (5 N) from ChemCraft Ltd. and an in-house synthesized $PbBr_2$ were used as reactants. These were mixed in an equimolar ratio loaded into a quartz tube, carefully evacuated, and sealed with a flame. This ampoule was placed in a muffle furnace, heated to 650°C, and held for 5 h to complete the reaction. Removal of the $CsPbBr_3$ is done by breaking the ampoule.
2. *Substrate preparation*: Patterned fluorine doped tin-oxide (FTO) coated glass slices with additional TiO_2 coating are used as substrates. The FTO pattering is done by an electrochemical reduction of the FTO to metallic tin, which lifts off from the glass. To define the etching area, a positive photoresist is applied by spin coating and is structured by photolithography. The patterned FTO consists of six 0.5 mm wide stripes along the substrate. The substrate preparation is finalized by spin-coating of a TiO_2 suspension (Solaronixs Ti-Nanoxide BL/SC) and a post-annealing step at 550°C for 60 min. This results in a compact TiO_2 film with a thickness of 50–70 nm. Before each preparation step, the substrates are cleaned in an O_3 plasma oven.
3. *Confined melting of $CsPbBr_3$*: utilized a furnace (EFCO 110) equipped with a camera and a K-type thermocouple at the sample position. A Raspberry Pi controls a phase-fired regulator that powers the oven, measures the temperature of the thermocouple, and records video from a camera connected to its CSI bus. Between the substrates, 70 mg $CsPbBr_3$ is deposited. At ∼570°C the $CsPbBr_3$ melts, followed by a cooling cycle to RT in ∼2 h.

4.2 | Scanning electron microscopy (SEM)

Uses a Quanta 200F microscope (Thermo Fisher Scientific). It operated at an acceleration voltage $V_{acc} = 5\,\text{kV}$ and the images are recorded with the secondary electron detector.

4.3 | Absorption spectroscopy

Uses a Jasco V-670 double-beam spectrometer. The molten $CsPbBr_3$ layer thickness is reduced to 4 μm to enable a measurement beyond the bandgap.

4.4 | Transient photocurrent and time-of-flight

The excitation source is a solid-state laser (BDL-488-SMN from Becker & Hickl GmbH) emitting at 488 nm, pulse-width 40–90 ps, 6.5 pJ. The pulse energy is measured with a power meter from Ophir Optronics at the sample position. The photocurrent is amplified with a high-speed voltage amplifier (Femto HSA-X-I-2-40) with an input impedance of 50 Ohm. The tr-PC traces are recorded with a Tektronix oscilloscope at a sampling rate of 12.5 GS s^{-1}. For the "balanced operational mode" experiment, an additional 50:50 beamsplitter is inserted and the sample is mounted on a 2 m long rail to adjust the individual laser beam path lengths. For ToF, the same setup is used with an additional function generator to apply the bias.

4.5 | Noise measurements

The electromagnetically shielded sample is connected to a low noise Femto DLPCA-200 transimpedance amplifier with an amplification of 10^{11} V A^{-1} and a -3 dB roll-off at 1 kHz. A Stanford Research Systems SR770 FFT Spectrum Analyzer with its internal FFT provides the noise power density-spectrum.

4.6 | Optical-pump and THz-Probe (OPTP)

The sample is photoexcited with pulses from an amplified ultrafast laser system (∼35 fs pulse duration, 800 nm central wavelength, 5 kHz repetition rate Ti:Sapphire laser system from Spectra Physics: MaiTai–Ascend–Spitfire regenerative amplifier) that were frequency-doubled to 400 nm wavelength with a 1 mm thick BBO crystal. The fluence of the pump pulse is controlled with a variable ND filter wheel. The relative time delays between pump and probe pulses were set using optical delay stages, and the sample is illuminated with THz radiation generated with a tri-layer spintronic emitter (2 nm tungsten, 1.8 nm $Co_{40}Fe_{40}B_{20}$, 2 nm platinum on quartz substrate) after photoexcitation. The THz pulse is focused onto the sample using off-axis parabolic gold-coated mirrors. The transmitted THz radiation is detected by electro-optic sampling in a 1 mm-thick (110)-ZnTe crystal with an 800 nm gate beam. The polarization of the gate beam is measured using a quarter-wave plate, polarizing beam splitter and a balanced photodiode detector. THz transmission is detected using a lock-in technique implemented on a custom-made, field-programmable gate array-based data acquisition board. The sample is held under a vacuum.

4.7 | Time-resolved microwave conductivity (TRMC) and transient photoluminescence (tr-PL)

The sample is photoexcited using the same laser system as for OPTP. The initially generated microwave radiation (34 GHz) from a signal generator is converted to 102 GHz using a frequency tripler and subsequently launched via a standard gain feed horn antenna into free space. Utilizing PTFE lenses, the microwave radiation is focused onto the sample, with the transmitted radiation re-focused onto a custom-made GaAs Schottky-diode detector. An in-house fabricated broad-band amplifier amplifies photoinduced changes in the signal, with the signal then being measured with a fast oscilloscope. The TRMC system is calibrated with a sample of known photoconductivity. Used in conjunction with an in-house fabricated broad-band amplifier and recorded on the same oscilloscope as above, a fast photodiode detector measures the tr-PL response of the sample. The time resolution of the system is 1.1 ns for TRMC transients and 2.6 ns for tr-PL transients.

ACKNOWLEDGMENTS

The work at ETH Zürich was financially supported by the Swiss Innovation Agency (Innosuisse) under grant agreement 46894.1 IP-ENG and by ETH Zürich through the ETH + Project SynMatLab: Laboratory for Multiscale Materials Synthesis. J.R.S.L. thanks Oxford Photovoltaics Ltd. for additional support as part of an EPSRC Industrial CASE studentship. V.J.-Y.L thanks Oxford Photovoltaics Prosperity Partnership and Rank Prize Return to Research Grant for financial support. Open access publishing facilitated by Eidgenossische Technische

Hochschule Zurich, as part of the Wiley - Eidgenossische Technische Hochschule Zurich agreement via the Consortium Of Swiss Academic Libraries.

CONFLICT OF INTEREST STATEMENT

The authors declare no conflict of interest.

DATA AVAILABILITY STATEMENT

The data that support the findings of this study are available from the corresponding author upon reasonable request.

ORCID

Sergii Yakunin https://orcid.org/0000-0002-6409-0565

REFERENCES

1. Li N, Ho CP, Xue J, et al. A progress review on solid-state LiDAR and nanophotonics-based LiDAR sensors. *Laser Photon Rev*. 2022;16:24.
2. Heide F, Diamond S, Lindell DB, Wetzstein G. Sub-picosecond photon-efficient 3D imaging using single-photon sensors. *Sci Rep*. 2018;8(1):17726.
3. Shrestha S, Matt GJ, Osvet A, Niesner D, Hock R, Brabec CJ. Assessing temperature dependence of drift mobility in methylammonium Lead iodide perovskite single crystals. *J Phys Chem C*. 2018;122(11):5935-5939.
4. Yamada Y, Kanemitsu Y. Electron-phonon interactions in halide perovskites. *NPG Asia Mater*. 2022;14(1):48.
5. Sakhatskyi K, Turedi B, Matt GJ, et al. Stable perovskite single-crystal X-ray imaging detectors with single-photon sensitivity. *Nat Photon*. 2023;17(6):510-517.
6. Brandt RE, Stevanović V, Ginley DS, Buonassisi T. Identifying defect-tolerant semiconductors with high minority-carrier lifetimes: beyond hybrid lead halide perovskites. *MRS Commun*. 2015;5(2):265-275.
7. Stoumpos CC, Kanatzidis MG. Halide perovskites: poor man's high-performance semiconductors. *Adv Mater*. 2016;28(28):5778-5793.
8. Green MA, Ho-Baillie A, Snaith HJ. The emergence of perovskite solar cells. *Nat Photon*. 2014;8(7):506-514.
9. He Y, Matei L, Jung HJ, et al. High spectral resolution of gamma-rays at room temperature by perovskite $CsPbBr_3$ single crystals. *Nat Commun*. 2018;9(1):1609.
10. Shrestha S, Fischer R, Matt GJ, et al. High-performance direct conversion X-ray detectors based on sintered hybrid lead triiodide perovskite wafers. *Nat Photon*. 2017;11(7):436-440.
11. Zhao X, Wang S, Zhuge F, et al. High-performance planar-type photodetector based on hot-pressed $CsPbBr_3$ wafer. *J Phys Chem Lett*. 2022;13(13):3008-3015.
12. Matt GJ, Levchuk I, Knüttel J, et al. Sensitive direct converting X-ray detectors utilizing crystalline $CsPbBr_3$ perovskite films fabricated via scalable melt processing. *Adv Mater Interfaces*. 2020;7(4):1901575.
13. Sakhatskyi K, Bhardwaj A, Matt GJ, Yakunin S, Kovalenko MV. A decade of Lead halide perovskites for direct-conversion X-ray and gamma detection: technology readiness level and challenges. *Adv Mater*. 2025;37(27):2418465.
14. Tsarev S, Proniakova D, Liu X, et al. Vertically stacked monolithic perovskite colour photodetectors. *Nature*. 2025;642(8068):592-598.
15. Shen L, Fang Y, Wang D, et al. A self-powered, sub-nanosecond-response solution-processed hybrid perovskite photodetector for time-resolved photoluminescence-lifetime detection. *Adv Mater*. 2016;28(48):10794-10800.
16. Morteza Najarian A, Vafaie M, Johnston A, et al. Sub-millimetre light detection and ranging using perovskites. *Nat Electron*. 2022;5(8):511-518.
17. Dekorsy T, Pfeifer T, Kütt W, Kurz H. Subpicosecond carrier transport in GaAs surface-space-charge fields. *Phys Rev B*. 1993;47(7):3842-3849.
18. Héroux JB, Kuwata-Gonokami M. Photoexcited carrier dynamics in InAs, GaAs, and InSb probed by terahertz excitation spectroscopy. *Phys Rev Appl*. 2017;7:054001.
19. Stoumpos CC, Malliakas CD, Peters JA, et al. Crystal growth of the perovskite semiconductor $CsPbBr_3$: a new material for high-energy radiation detection. *Cryst Growth Des*. 2013;13(7):2722-2727.
20. Chung DY, Lin W, Unal M, et al. Growth of high-purity $CsPbBr_3$ crystals for enhanced gamma-ray detection. *Cryst Growth des*. 2024;24(22):9590-9600.
21. Zanatta AR. Revisiting the optical bandgap of semiconductors and the proposal of a unified methodology to its determination. *Sci Rep*. 2019;9(1):11225.
22. Koiry SP, Jha P, Veerender P, et al. An electrochemical method for fast and controlled etching of fluorine-doped tin oxide coated glass substrates. *J Electrochem Soc*. 2017;164(2):E1-E4.
23. Kanak A, Kopach O, Kanak L, et al. Melting and crystallization features of $CsPbBr_3$ perovskite. *Cryst Growth Des*. 2022;22(7):4115-4121.
24. Tiwana P, Parkinson P, Johnston MB, Snaith HJ, Herz LM. Ultrafast terahertz conductivity dynamics in mesoporous TiO_2: influence of dye sensitization and surface treatment in solid-state dye-sensitized solar cells. *J Phys Chem C*. 2010;114(2):1365-1371.
25. Righetto M, Wang Y, Elmestekawy KA, et al. Cation-disorder engineering promotes efficient charge-carrier transport in $AgBiS_2$ nanocrystal films. *Adv Mater*. 2023;35(48):202305009.
26. Ulatowski AM, Elmestekawy KA, Patel JB, et al. Contrasting charge-carrier dynamics across key metal-halide perovskite compositions through in situ simultaneous probes. *Adv Funct Mater*. 2023;33(51):202305283.
27. Herz LM. Charge-carrier dynamics in organic-inorganic metal halide perovskites. *Annu Rev Phys Chem*. 2016;67(1):65-89.
28. Seifert T, Jaiswal S, Martens U, et al. Efficient metallic spintronic emitters of ultrabroadband terahertz radiation. *Nat Photon*. 2016;10(7):483-488.
29. Nienhuys H-K, Sundström V. Intrinsic complications in the analysis of optical-pump, terahertz probe experiments. *Phys Rev B*. 2005;71(23):235110.
30. Bednorz M, Matt GJ, Głowacki ED, et al. Silicon/organic hybrid heterojunction infrared photodetector operating in the telecom regime. *Org Electron*. 2013;14(5):1344-1350.
31. Pope M, Swenberg CE. *Electronic Processes in Organic Crystals and Polymers*. Oxford University Press; 1999.
32. Kasap SO. *Photoconductivity and Photoconductive Materials*. Wiley; 2022:179-251.
33. Belas E, Betušiak M, Karuppaiya M, Grill R, Praus P. *2024 IEEE Nuclear Science Symposium (NSS), Medical Imaging*

Conference (MIC) and Room Temperature Semiconductor Detector Conference (RTSD). IEEE; 2024.
34. Almora O, Matt GJ, These A, et al. Surface versus bulk currents and ionic space-charge effects in $CsPbBr_3$ single crystals. *J Phys Chem Lett*. 2022;13(17):3824-3830.
35. Yan H, Cao G, Wang J, et al. Uncovering the modest hole mobility for the intrinsic single crystal $CsPbBr_3$ by variable-temperature time of flight measurement. *Appl Phys Lett*. 2025; 126(12):122105.
36. Kočka J, Nebel CE, Abel CD. Solution of the μτ problem in a-Si: H. *Philos Mag B*. 1991;63(1):221-246.
37. Hornbeck JA, Haynes JR. Trapping of minority carriers in silicon. I.P-type silicon. *Phys Rev*. 1955;97(2):311-321.
38. Protesescu L, Yakunin S, Bodnarchuk MI, et al. Nanocrystals of cesium Lead halide perovskites ($CsPbX_3$, X = Cl, Br, and I): novel optoelectronic materials showing bright emission with wide color gamut. *Nano Lett*. 2015;15(6):3692-3696.
39. Crothers TW, Milot RL, Patel JB, et al. Photon reabsorption masks intrinsic bimolecular charge-carrier recombination in $CH_3NH_3PbI_3$ perovskite. *Nano Lett*. 2017;17(9):5782-5789.
40. Davies CL, Filip MR, Patel JB, et al. Bimolecular recombination in methylammonium lead triiodide perovskite is an inverse absorption process. *Nat Commun*. 2018;9(1):293.
41. Regan BO, Grätzel M. A low-cost, high-efficiency solar cell based on dye-sensitized colloidal TiO_2 films. *Nature*. 1991; 353(6346):737.
42. Beljonne D, Cornil J, eds. *Multiscale Modelling of Organic and Hybrid Photovoltaics*. Springer Berlin Heidelberg; 2014.
43. Haynes JR, Shockley W. The mobility and life of injected holes and electrons in germanium. *Phys Rev*. 1951;81(5):835-843.
44. Smith RA. *Semiconductors*. Cambridge University Press; 1964.

SUPPORTING INFORMATION

Additional supporting information can be found online in the Supporting Information section at the end of this article.

How to cite this article: Matt GJ, Bartosh V, Lilly JRS, et al. Perovskite-based time-domain signal-balancing LiDAR sensor with centimeter depth resolution. *InfoMat*. 2025;e70104. doi:10.1002/inf2.70104